PAPER

Check for updates

Promotion of phenol photodegradation based on novel self-assembled magnetic bismuth oxyiodide core–shell microspheres†

Danlin Qian, Suting Zhong, Suyun Wang, Yaru Lai, Nan Yang and Wei Jiang [iD] *

A novel visible-light driven "plates-over-nanospheres" (PONs) photocatalyst with BiOI nanoplates grown on the surface of Fe_3O_4 nanospheres was prepared using a facile method. By utilizing the self-assembly of the BiOI nanoplates, this environmentally friendly method challenges the classic synthesis of core–shell heterojunctions which always includes tedious synthesis steps as well as linker shells. With the introduction of magnetic cores, the PONs promoted the favorable degradation of phenol under visible-light irradiation. The enhanced visible-light photocatalytic performance of the PONs was ascribed to the unique synergistic effect between the magnetic cores and BiOI shells, resulting in the improved separation and inhibited recombination of photogenerated carriers. Moreover, the PONs maintained nearly constant photodegradation rates even after five cycles of photocatalytic experiments, without obvious catalyst deactivation. All in all, our work paves a novel way for the further design of heterojunction photocatalysts with fine recyclability and enhanced photocatalytic activity.

1. Introduction

As a promising environmental remediation technology, photocatalysts have attracted considerable attention since they were first investigated about 40 years ago.[1] Up to now, there has been a lot of research into the purification of wastewater, especially the removal of toxic organic contaminants.[2–4] Despite significant efforts to date, the semiconductor photocatalysis technology is still insufficient to satisfy the requirements for industrially oriented applications due to two intrinsic shortcomings of the conventional photocatalytic systems. One is the wide band gaps, for example light absorption by TiO_2 is limited to ultraviolet light (about 4% of the solar spectrum), making it possess only moderate photocatalytic performance.[5–8] The other shortcoming is the complexity of catalyst separation and recovery. Once finishing their mission in the liquid phase, powder-like photocatalysts are always difficult to separate and recover. Therefore, research into the construction of high efficiency and recyclable visible-light driven photocatalysts is the focus of much endeavor under the increasing environmental pressure.[9–11]

The past ten years have witnessed an increasing interest in bismuth-based oxides, and this research is mainly focused on

BiOX (X = I, Br, Cl),[12–17] Bi_2WO_6,[18,19] $BiVO_4$,[20–24] BiO_2CO_3,[25] Bi_2MoO_6,[26,27] *etc.* Among these, BiOX is generally accepted to be a promising photocatalytic material because of its excellent photocarrier mobility, owing to its layered morphology of interlacing $[Bi_2O_2]^{2+}$ slabs and halogen atoms. In the family of bismuth oxyhalides, BiOI is proven to be the most promising photocatalyst candidate for wastewater treatment, having the narrowest band gap (*ca.* 1.6–1.9 eV) and the strongest visible-light absorption.[28–30] However, the suspended particulate catalysts are difficult to recover, which limits the functional life-time of BiOI for photocatalysis in practical applications. Moreover, the loss of the photocatalyst during the photocatalytic reaction and separation process may even cause secondary pollution. Given this situation, it is of crucial significance to construct heterogeneous systems and overcome the above recycling drawback inherent to single phase photocatalysts.

Attempts have been made to introduce magnetic-functional components into photocatalytic material.[31,32] As a commonly used magnetic material in industrial manufacture, Fe_3O_4 is similar to a conductor due to its narrow band gap (0.1 eV).[33] So far, many studies have proved that Fe_3O_4 could be used as a favorable co-catalyst to transfer photogenerated electron–hole pairs, and that it could even offer beneficial synergistic effects with the photocatalyst, rendering it of significance for photocatalytic purposes.[34,35] However, the synthesis of special core–shell orientated composites is always complicated and costly, due to the introduction of some linker layers (*e.g.* silica, polymers) as well as the required tedious intermediate steps.[36] Additionally, the saturation magnetization (M_s) of composite materials can be weakened by the existence of linker layers.

National Special Superfine Powder Engineering Research Center of China, School of Chemical Engineering, Nanjing University of Science and Technology, Nanjing 210094, China. E-mail: superfine_jw@126.com; Fax: +86 25 84315042; Tel: +86 25 84315042

Herein, a novel and facile synthesis of BiOI nanoplates stacked on Fe_3O_4 nanospheres (PONs) was employed without the use of any linker shell. It is worth noting that in this study, phenol could be degraded within 5 h using this photocatalyst, and PONs showed good recyclability. Additionally, the formation process of the composites, as well as their corresponding optical properties, electrochemical properties and photocatalytic mechanism were investigated in detail. The rational design is a proof of concept for integrating functional magnetic material with photocatalysts and even provides an alternative for the destruction of phenol.

2. Experimental

2.1 Materials

All chemicals were of analytical grade, commercially available and used without purification. Bismuth nitrate pentahydrate ($Bi(NO_3)_3 \cdot 5H_2O$), ferric chloride ($FeCl_3 \cdot 6H_2O$) and potassium iodide (KI) were purchased from Sinopharm Chemical Reagent Co. Ltd. Other chemicals were all obtained from Shanghai Ling Feng Chemical Reagent Co. Ltd.

2.2 Synthesis of PONs

PONs were synthesized *via* a first-step solvothermal process and a second-step chemical precipitation treatment. During the first-step solvothermal process, porous magnetite Fe_3O_4 nanospheres were prepared according to the reported strategy.[37] For the preparation of PONs, $Bi(NO_3)_3 \cdot 5H_2O$ (2 mmol) was next dissolved in ethylene glycol (EG) solution and ethanol solution, and the volume ratio of EG to ethanol was controlled at 1/2. To ensure all materials were dissolved completely, the mixture was stirred for 30 min at least. Then certain stoichiometric amounts of Fe_3O_4 powders were added into the solution under ultrasonication to give homogeneous dispersion systems. The samples are denoted as $PONs_{(x/y)}$, in which x/y is the molar ratio of Fe/Bi. After that, KI (2 mmol) solution was added dropwise into the above mixtures. Subsequently, 1.5 M $NH_3 \cdot H_2O$ was added to adjust the pH value to ~7.0 and then the suspensions

were stirred constantly at 80 °C for 3 h. Finally, the resulting precipitates were collected, washed thoroughly with ethanol and deionized water three times, and then dried at 40 °C in a vacuum oven. The formation procedure of the PONs is illustrated in Fig. 1.

2.3 Characterization

The phase structure information of the samples was obtained by X-ray diffraction (XRD) on a D8 Advance diffractometer (Bruker, Germany) with Cu Kα radiation ($\lambda = 0.154$ nm). The microstructure and morphology of the samples were investigated by S-4800 scanning electron microscopy (SEM, Hitachi, Japan) and high resolution transmission electron microscopy (HRTEM, Tecnai G2 F30 S-TWIN). UV-vis diffuse reflectance spectroscopy (DRS) of the samples was performed with a UV-vis spectrophotometer (UV-2700, Shimadzu). For the DRS sample preparation, the powders were made as dry-pressed films with $BaSO_4$ as the reflectance standard. Surface chemical compositions and states were obtained from X-ray photoelectron spectroscopy (XPS, K-Alpha, Thermo VG). The magnetic properties were characterized by a vibrating sample magnetometer (VSM, Lakeshore-735) at room temperature. Fourier transform infrared (FT-IR) spectra of the samples were measured on an FT-IR spectrometer (Nicolet 6700). The photoluminescence (PL) spectra of the samples were characterized using a fluorescence spectrophotometer (Shimadzu RF6000, Japan). N_2 absorption/desorption isotherms were calculated by Micromeritics ASAP 2020 according to the Brunauer–Emmett–Teller (BET) method.

2.4 Photocatalytic evaluation

The photocatalytic performances of the as-prepared samples were monitored by degradation of phenol and methyl orange (MO) under visible-light irradiation (500 W, $\lambda > 420$ nm) at ambient temperature. All photocatalytic tests were performed using the same initial conditions: the photocatalyst (50 mg) was added into 50 mL of organic reaction solution (20 mg L^{-1}). Prior to photoreaction, the suspension solution was continuously stirred in the dark to guarantee an absorption–desorption equilibrium between the degrading pollutants and the photocatalysts. Throughout the reaction, at appropriate intervals, about 3 mL of the reaction suspension was sampled and magnetically separated to remove the solid. Active-species trapping experiments were performed with the introduction of diverse quenchers. The concentrations of supernatant liquids were measured by monitoring the characteristic absorption bands (269 nm for phenol, 465 nm for MO, respectively), with an UV-vis spectrophotometer (Agilent Technologies Cary 100).

2.5 Photoelectrochemical measurements

Typically, the aqueous dispersions of the as-prepared samples were dip coated on indium-tin oxide glasses (ITO), yielding electrodes with catalyst loading areas of 1 cm^2. The photocurrent *vs.* time curves were measured by an electrochemical work station (CHI760E, Shanghai, China) in a standard 3-electrode system with the ITO electrode as the working electrode, a Pt wire as the counter electrode and an Ag/AgCl electrode as the
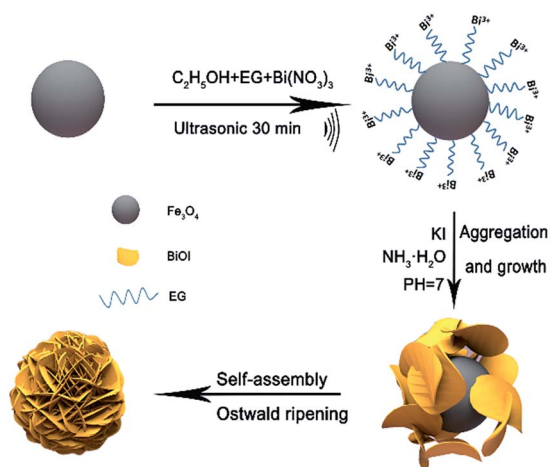

Fig. 1 Schematic illustration of the formation procedure for PONs.

reference electrode under a constant bias of 1.23 V *vs.* RHE. The power intensity of the incident light was adjusted to 100 mW cm^{-2}. Electrochemical impedance spectroscopy (EIS) was carried out in the frequency range of 10^{-2} to 10^5 Hz with an amplitude of 5 mV at the open circuit potential. Mott–Schottky analysis was employed with an amplitude of 5 mV *vs.* the Ag/ AgCl reference electrode.

2.6 $\cdot O_2^-$ and $\cdot OH$ active species trapping and quantification experiments

For detecting the active species during photocatalytic reaction, superoxide radicals ($\cdot O_2^-$), hydroxyl radicals ($\cdot OH$), and holes (h^+) were investigated by adding 1.0 mM benzoquinone (BQ, a quencher of $\cdot O_2^-$), 1 mM methanol (a quencher of $\cdot OH$) or 1 mM disodium ethylene-diaminetetraacetate (EDTA-2Na, a quencher of h^+), respectively.[38] The quantitative amount of $\cdot O_2^-$ and $\cdot OH$ generated were inspected by nitroblue tetrazo-lium (NBT) transformation and terephthalic acid photo-luminescence (TA-PL) probing, respectively.[39] The production of $\cdot O_2^-$ was quantitatively analyzed by recording the concentration of NBT since NBT can react with $\cdot O_2^-$ and displays a maximum absorbance at 260 nm. Terephthalic acid (TA) can react with $\cdot OH$ to transform 2-hydroxyterephthalic acid (TA-OH), which is a highly fluorescent product. By monitoring the PL intensity of TA-OH (excitation at 315 nm), the production of $\cdot OH$ was quantitatively analyzed.

3. Results and discussion

3.1 Characterization of structure and properties of PONs

The phase composition of the as-prepared $PONs_{(1/3)}$, Fe_3O_4 and BiOI samples are exhibited in Fig. 2a. All of the diffraction peaks in the Fe_3O_4 and BiOI samples could be perfectly indexed to the cubic Fe_3O_4 phase (JCPDS no: 19-0629) and the tetragonal BiOI phase (JCPDS no: 73-2062), indicative of the production of pure BiOI and Fe_3O_4. As shown in Fig. 2a, XRD peaks of tetragonal BiOI could be clearly observed in the PONs, and the diffraction peak at 35.4° corresponded to the (311) crystalline plane of Fe_3O_4, confirming the co-existence of Fe_3O_4 and BiOI in the composite. Besides, no miscellaneous peaks were observed in the sample, indicating the high purity of the composite.

The chemical composition and chemical bonding of the as-prepared samples were studied by the FT-IR investigation. As shown in Fig. 2b, the main absorption band of $PONs_{(1/3)}$ located at approximately 484 cm^{-1} could be attributed to the symmet-rical A_{2u}-type vibration mode of the Bi–O bond.[40] The FT-IR spectra of both pure BiOI and $PONs_{(1/3)}$ contain characteristic absorption bands at 3411 cm^{-1} and 1620 cm^{-1}, which were assigned to the stretching vibration and bending vibration of surface O–H respectively. The peak at 1382 cm^{-1} was assigned to the O–H deformations of the C–OH groups. Additionally, the slight absorptions at 2943 cm^{-1} and 2875 cm^{-1} could be attributed to C–H groups. These observed peaks could be derived from EG adsorbed on the surface of the photocatalyst in the synthetic process. All of the characteristic peaks of BiOI are retained in the $PONs_{(1/3)}$, indicating that the addition of Fe_3O_4
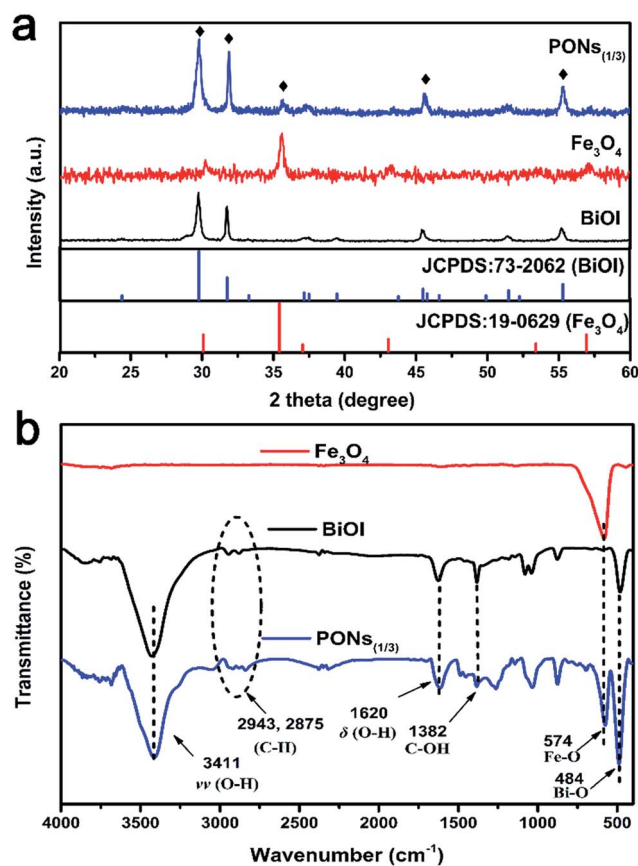

Fig. 2 (a) XRD patterns of $PONs_{(1/3)}$, Fe_3O_4 and BiOI; (b) FT-IR spectra of $PONs_{(1/3)}$, Fe_3O_4 and BiOI.

had no effect on the chemical structure of BiOI in the composites. Moreover, the spectrum of $PONs_{(1/3)}$ exhibits a band at 574 cm^{-1}, as a result of the stretching vibration of Fe–O bonds in the Fe_3O_4. The above results indicate that the $PONs_{(1/3)}$ are composed of bismuth oxyiodides and Fe_3O_4. No impurity absorption peak was detected, which is in accordance with the XRD result.

To observe the morphology of PONs and reveal the formation process of the core–shell structure in detail, time-dependent experiments were carried out and the products were investi-gated by SEM. The composites with different reaction times of 0 h, 1 h, 2 h and 3 h in the water-bath are denoted as PONs-0, PONs-1, PONs-2 and PONs-3, respectively. As shown in Fig. 3a1, the Fe_3O_4 nanospheres had an average diameter of 400 nm and a relatively rough surface. Sheet-shaped structures of BiOI were randomly distributed around the Fe_3O_4 magnetic core. After a reaction time of 1 h (Fig. 3b1 and b2), underde-veloped hierarchical architectures existed with some individu-ally dispersed nanoplates, indicating that the oriented attachment was still in progress. When the reaction time was prolonged to 2 h (Fig. 3c1 and c2), separate nanoplates faded away and large scale cabbage-shaped hierarchical architectures were formed. As the reaction went further, the BiOI nanoplates were regularly assembled over the magnetic cores, and fully developed. 3D flowerlike PONs with diameters of 1 μm were
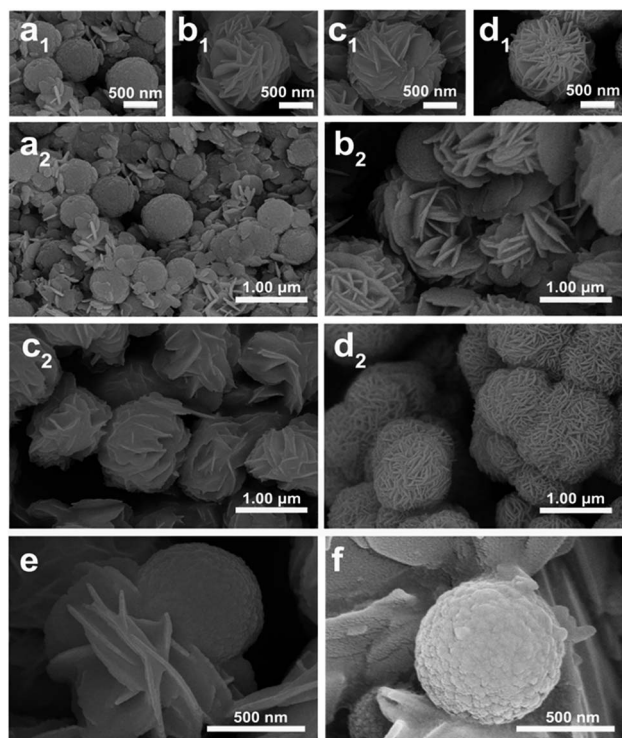
Fig. 3 SEM images (a1, a2) of PONs-0, (b1, b2) of PONs-1, (c1, c2) of PONs-2, (d1, d2, e) of PONs-3, and (f) of the Fe_3O_4/BiOI composite.
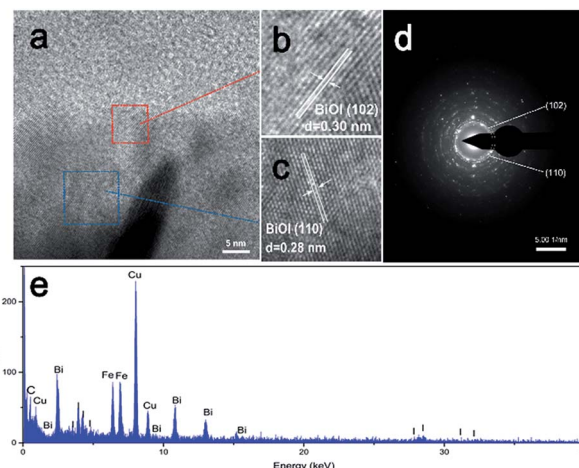

Fig. 4 (a–c) HRTEM images of PONs; (d) SAED pattern of PONs; (e) EDX spectrum of PONs.

Table 1 Results of specific surface areas, pore volumes and average pore diameters for $PONs_{(1/3)}$, EBiOI, HBiOI and Fe_3O_4/BiOI

Samples	S_{BET} (m^2 g^{-1})	V_{pore} (cm^3 g^{-1})	Average pore diameter (nm)
$PONs_{(1/3)}$	46.60	0.149	10.891
EBiOI	8.84	0.033	8.388
HBiOI	2.77	0.011	3.560
Fe_3O_4/BiOI	2.90	0.012	4.357

eventually formed after the 3 h water-bath reaction (Fig. 3d1 and d2). Although very few microspheres were not fully encapsulated (Fig. 3e), their presence proves the existence of the core–shell structure intuitively. Additionally, the good interface between BiOI and Fe_3O_4 suggests that the nanoplates were compatible with the magnetic core. In the contrast experiment, the direct reaction of Bi(NO$_3$)$_3 \cdot$5H$_2$O, KI and Fe_3O_4 in aqueous solution (Fe_3O_4/BiOI) resulted in Fe_3O_4 nanospheres randomly loaded on irregular large plates of BiOI with no distinct trend to form core–shell hierarchical nanostructures (Fig. 3f).

Detailed structural information about the $PONs_{(1/3)}$ was further obtained by HRTEM, selected area electron diffraction (SAED) and electron dispersive spectroscopy (EDX). Fig. 4a shows a typical HRTEM image of a BiOI shell, which reveals the highly crystalline nature of the composites. As shown in Fig. 4b and c, the spacings of the adjacent lattice fringes were ca. 0.30 and 0.28 nm, which correspond to the interplanar spacings of the (102) plane and (110) plane of tetragonal BiOI, respectively. Fig. 4d shows that in the SAED patterns of the composite, electron diffraction spots could be indexed to the (102) and (110) planes of BiOI, indicating a good agreement with the HRTEM observations. EDX analysis (Fig. 4e) reveals the existence of C, Bi, O, I and Fe on the $PONs_{(1/3)}$ composites. These results further corroborate the successful synthesis of PONs and are consistent with the observations from XRD and SEM.

To gain more insight into the specific surface areas and the porous structures of the samples, BET was conducted. In Table 1, the corresponding BET surface areas of HBiOI and Fe_3O_4/BiOI were as low as 2.77 m^2 g^{-1} and 2.90 m^2 g^{-1} respectively.

The isotherm of the as-prepared Fe_3O_4/BiOI and HBiOI are close to Type III without a hysteresis loop at high relative pressure, suggesting the compact structure of HBiOI and Fe_3O_4/BiOI. It can be speculated that Fe_3O_4 does not play a role in increasing the BET surface area in the Fe_3O_4/BiOI, where Fe_3O_4 nanospheres are randomly loaded on irregular large plates of BiOI. Conversely, the BET surface area of $PONs_{(1/3)}$ was measured to be 46.60 m^2 g^{-1}, which is significantly higher than that of pristine EBiOI (BiOI prepared in an alcohol solvent solution system) with a BET surface area of 8.84 m^2 g^{-1}, confirming the supporting role of Fe_3O_4 cores. Moreover, the isotherm of the as-prepared $PONs_{(1/1)}$, and EBiOI are close to Type IV with a distinct H3 hysteresis loop at a high relative pressure between 0.6 and 1.0.[41] The behavior shows the predominance of mesopores in the microspheres. As shown in Fig. 5b (inset), the pore volume and size of $PONs_{(1/1)}$ are 0.149 cm^3 g^{-1} and 10.891 nm, respectively, which are slightly larger than the corresponding measurements for other samples. The slit-like pores are generally formed by the aggregation of plate-like particles, which is consistent with the self-assembled nanoplate-like morphology observed in the SEM results.[42] Generally, a larger specific surface area and pore volume correspond to more surface active sites exposed and available to the reaction,[43] which in turn results in better adsorption, desorption and diffusion of reactants. Therefore, the large specific surface area as well as pore volume might be responsible for the high photocatalytic activity of the $PONs_{(1/3)}$.
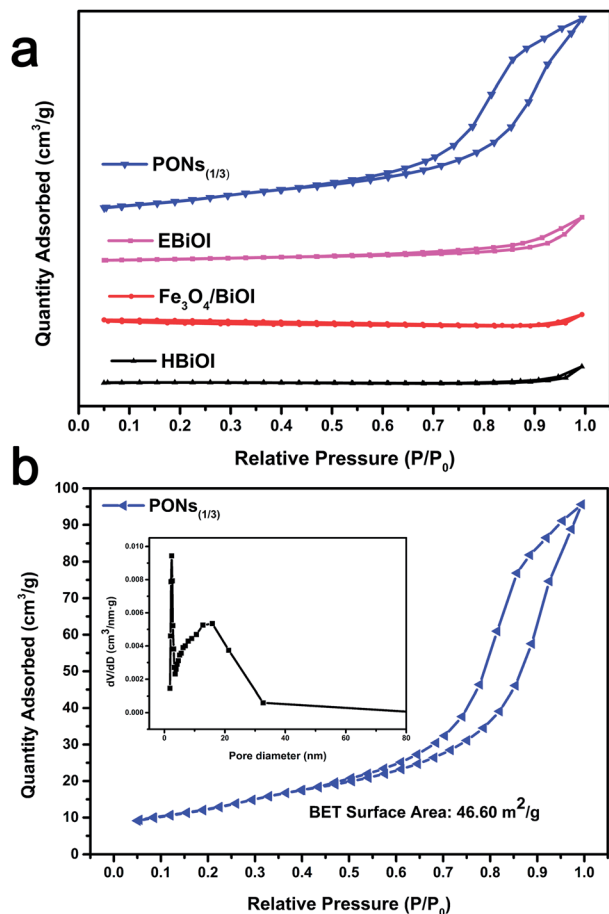
Fig. 5 (a) N_2 adsorption–desorption isotherm distribution curves for as-prepared PONs$_{(1/1)}$, EBiOI, Fe$_3$O$_4$/BiOI and HBiOI. (b) Enlarged view of PONs$_{(1/3)}$ and pore size distribution of PONs$_{(1/3)}$ (inset).

The chemical composition and surface chemical states of the PONs$_{(1/3)}$ were further investigated by XPS. The peak positions were calibrated by referencing the C 1s line to 284.50 eV. As shown in Fig. 6a, the typical XPS survey spectrum indicated the existence of Bi, O, I, and C at the surface of PONs$_{(1/3)}$ and the carbon peak could be attributed to the surface adventitious carbon. Two symmetrical peaks at 159.13 and 164.48 eV in the spectrum of Bi 4f were respectively assigned to Bi 4f$_{7/2}$ and Bi 4f$_{5/2}$, indicating the existence of Bi^{3+} (Fig. 6b). The peaks at 619.78 and 631.28 eV in the spectrum of I 3d were respectively assigned to the inner electrons of I 3d$_{5/2}$ and 3d$_{3/2}$ (Fig. 6c).[13] Notably, Fe 2p peaks were not found in the high-resolution spectrum, which was attributed to the fact that the technique probes only the surface of a micrometer sphere and the magnetic core could not be detected.[44] This phenomenon indirectly proves that the Fe$_3$O$_4$ nanospheres were covered completely by BiOI shells. Meanwhile, the high-resolution XPS spectrum of O 1s (Fig. 6e) could be deconvoluted into two peaks at binding energies of 530.6 and 531.8 eV, which respectively correspond to Bi–O bonds of BiOI,[13] and O–H bonds of the surface-adsorbed water.[45]

Generally, the first step of photocatalysis for a semiconductor is the conversion of light into energetic electrons and
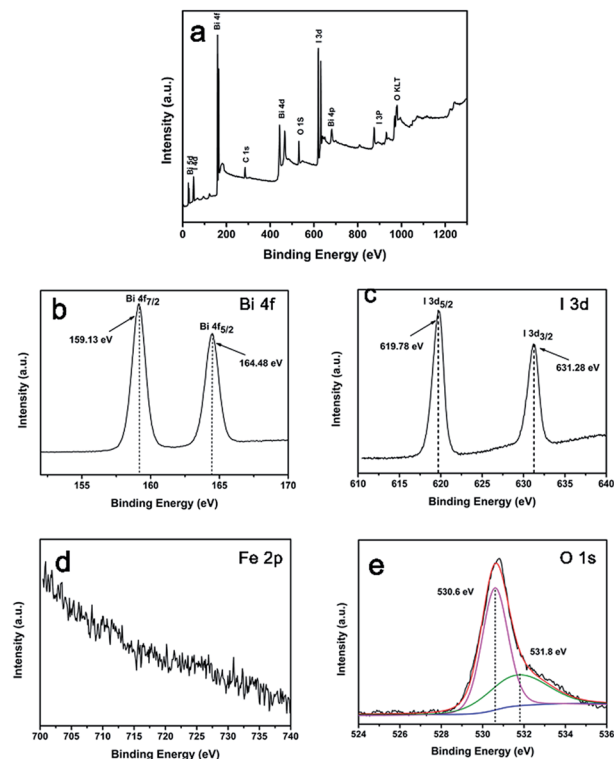

Fig. 6 XPS spectra of the as-prepared PONs$_{(1/3)}$ catalyst: (a) survey spectrum of the sample; (b) Bi 4f; (c) I 3d; (d) Fe 2p; and (e) O 1s.

holes.[46] For efficient photocatalytic activity, a wide spectrum of optical absorption is necessary. To further explore how the heterojunction influences the light absorption ability of PONs, we studied the optical properties of the as-prepared products by DRS. As shown in Fig. 7a, pure BiOI exhibited light absorption in the visible range and showed only one absorption edge at about 670 nm, whereas the light harvesting range of PONs$_{(1/3)}$ was slightly blue-shifted reaching to ~650 nm. As shown in
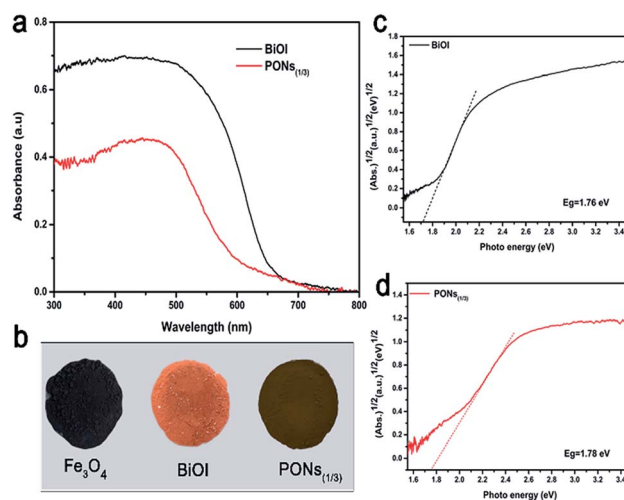

Fig. 7 (a) UV-vis diffuse reflectance spectra and (b) corresponding colors of pure Fe$_3$O$_4$, BiOI and PONs$_{(1/3)}$ samples. Plots showing the band gaps of (c) BiOI and (d) PONs$_{(1/3)}$ composites.

Fig. 7b, the color of BiOI was saffron and pure Fe_3O_4 was deep black. The slight blue shift of the absorption edge was in accordance with the color change from saffron (BiOI) to saddle brown ($PONs_{(1/3)}$). Nevertheless, $PONs_{(1/3)}$ still showed prominent absorbance in the visible-light range. The band gap (E_g) of a crystalline semiconductor follows the equation:[47]

$$\alpha h v = A(h v - E_g)^{n/2} \tag{1}$$

where α, v, A and h are absorbance, light frequency, a constant value and Planck's constant, respectively. For the indirect transition semiconductor BiOX, the value of n is 4.[17] The band gap of BiOX could be obtained from the plots of $(Abs)^{1/2}$ vs. hv; the intercepts of the tangents to the x-axis (hv) give an approximation of the band gap. Therefore, the E_g value of BiOI was calculated to be 1.76 eV (Fig. 7c), which is in accordance with the value reported in the literature.[16,47] Notably, as shown in Fig. 7d, the band gap of the $PONs_{(1/3)}$ composite was scarcely changed ($E_g = 1.78$ eV) despite the introduction of optically inactive Fe_3O_4, demonstrating that the heterojunction effect does not have a great influence on the optical absorption properties.

To further explore the correlation between synergistic effects and interfacial charge transfer, we carefully conducted transient photocurrent response measurements, EIS, and constructed the Mott–Schottky plots of the as-prepared products. As shown in Fig. 8a, under each 50 s on/off visible-light irradiation cycle, photocurrents with rapid and reproducible responses were generated. In comparison with pure BiOI, the $PONs_{(1/3)}$ electrode exhibited increased photocurrent density as well as more consistent photocurrent, demonstrating higher efficiency and lower recombination of photogenerated electron–hole pairs in the core–shell structures. The radius of the high frequency semicircle on an EIS spectrum mirrors the interface layer resistance of the material.[14] As shown in Fig. 8b, PONs showed

a smaller semicircle radius in its EIS Nyquist plot than pure BiOI at high frequency. This suggests that the presence of Fe_3O_4 can be a benefit to the interfacial charge transfer. To further determine the semiconductor type of the as-prepared product as well as its flat potential, Mott–Schottky analysis was employed herein. The positive or negative slope of a linear $1/C^2$ vs. potential curve implies the type of semiconductor. As shown in Fig. 8c, the linear slope for the $PONs_{(1/3)}$ catalyst is positive, indicating that it is an n-type semiconductor whose Fermi level (EF) is close to the conduction band (CB). Moreover, the flat-band potential of the binary $PONs_{(1/3)}$ composite, from the results at a frequency of 1000 Hz, is determined to be -0.85 V (1.23 eV vs. RHE). The above results indicate that an improved separation and an inhibited recombination of photogenerated carriers occur on the binary PONs composite, and further confirm that the improved photocatalytic performance can be attributed to this unique synergistic effect.

Additionally, PL spectroscopy was applied to elucidate the separation capacity of the photogenerated charge carriers and surface defects as shown in Fig. 8d. Generally, a lower intensity PL peak corresponds to a higher separation efficiency of electron and hole pairs, thus leading to a higher photocatalytic activity.[48] With emission peaks located at 446 nm, the room temperature PL spectra of the BiOI, $PONs_{(1/1)}$, $PONs_{(1/3)}$, $PONs_{(1/6)}$ and Fe_3O_4 samples are shown in Fig. 8d. The PL spectra show that pristine BiOI displays a more intense fluorescence emission peak than PONs. It can be speculated that the lower PL intensity of PONs is related to the good electrical conductivity of Fe_3O_4. The interfacial electrons efficiently transfer from the CB of BiOI to that of Fe_3O_4, hampering the recombination of photogenerated charge carriers. Moreover, it can be noticed that $PONs_{(1/3)}$ shows the lowest PL intensity when compared with $PONs_{(1/1)}$ and $PONs_{(1/6)}$, indicating that the ratio of Fe_3O_4 to BiOI is an important factor in the recombination of photogenerated charge carriers. Furthermore, the PL spectroscopy result perfectly matches the trend shown in the photocatalytic activity discussed previously, indicating that the recombination rate of electrons and holes could be suppressed greatly by the addition of Fe_3O_4.

3.2 Photocatalytic activity

To evaluate the photocatalytic efficiency of the as-prepared samples under visible-light irradiation, phenol with no indirect dye photosensitization was chosen to be a target pollutant. Fig. 9a shows the absorption spectra of phenol in the presence of $PONs_{(1/3)}$. The absorbance of phenol at 269 nm decreased sharply and almost disappeared after 5 hours, indicating that the $PONs_{(1/3)}$ possesses satisfactory photolysis efficiency. As shown in Fig. 9b, the influence of synthesis parameters such as the solvent system and the proportion of Fe_3O_4 were further investigated. Although BiOI has been considered as an excellent visible-light driven photocatalyst,[15] the BiOI random nanoplates (prepared in aqueous solution system, and denoted as HBiOI) displayed poor photocatalytic activity as did the BiOI microspheres (prepared in alcohol solvent solution system and denoted as EBiOI). The increased surface area and particle size
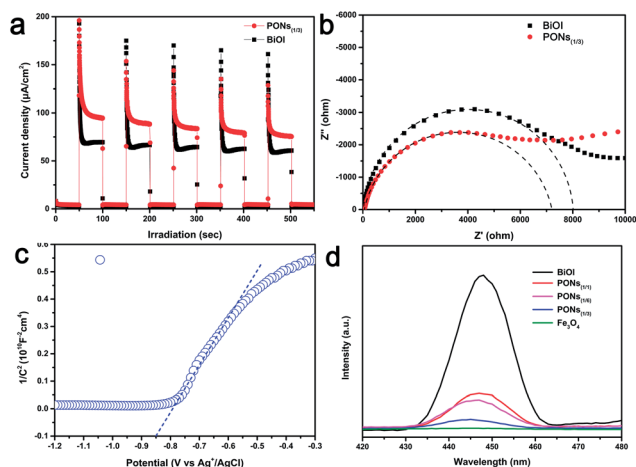

Fig. 8 (a) Photocurrent responses of BiOI and $PONs_{(1/3)}$ in 0.5 M Na_2SO_4 aqueous solutions (pH = 5.8) under irradiation with simulated sunlight at 1.23 V vs. RHE; (b) EIS Nyquist plots of pure BiOI and $PONs_{(1/3)}$; (c) flat potential determination of $PONs_{(1/3)}$ by Mott–Schottky plots; (d) PL spectra of BiOI, $PONs_{(1/3)}$, $PONs_{(1/1)}$, $PONs_{(1/6)}$ and Fe_3O_4.
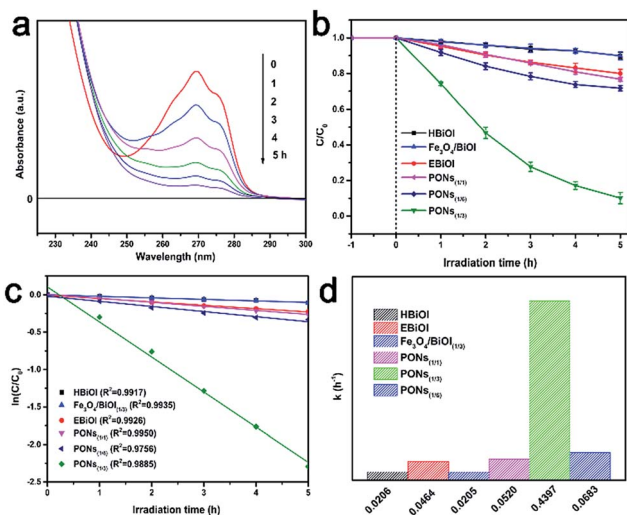
Fig. 9 (a) The time-dependent absorption spectra of phenol in the presence of PONs$_{(1/3)}$ under visible-light irradiation ($\lambda > 420$ nm). (b) Degradation ratios, (c) first-order kinetics data and (d) rate constants for the photocatalytic removal of phenol by various photocatalysts under visible-light irradiation.

Fig. 10 (a) Hysteresis loops of Fe$_3$O$_4$ and PONs$_{(1/3)}$ under a magnetic field at room temperature; (b) photodegradation of phenol over PONs$_{(1/3)}$ in successive cycles; (c) schematic diagram of sample recovery under an external magnetic field.

of EBiOI might account for the higher photocatalytic activity of this catalyst as compared to HBiOI,[17] although its activity was still much lower than that of PONs. To quantitatively explore the degradation rate of phenol, a pseudo-first order model was applied to the photocatalytic kinetic study.[49] It was found that the phenol photodegradation exhibits a good linear relationship (Fig. 9c). As shown from Fig. 9d, the rate constants k of HBiOI, EBiOI, Fe$_3$O$_4$/BiOI$_{(1/3)}$, PONs$_{(1/1)}$, PONs$_{(1/3)}$ and PONs$_{(1/6)}$ were respectively calculated to be 0.0206, 0.0464, 0.0205, 0.052, 0.4397 and 0.0683 h^{-1}. The optimal photocatalyst, PONs$_{(1/3)}$, could remove 90% phenol within 5 h and possessed the highest photocatalytic activity as compared to PONs$_{(1/1)}$ and PONs$_{(1/6)}$. It can be deduced that the proportions of the components affect the photocatalytic activity of PONs significantly. However, the removal of phenol over Fe$_3$O$_4$/BiOI$_{(1/3)}$ (mechanically mixed) upon visible-light irradiation was as low as 10%, indicating that the interaction between the BiOI and Fe$_3$O$_4$ also plays an important role in promoting photocatalytic efficiency.

The magnetic properties of the Fe$_3$O$_4$ nanospheres and PONs composite were measured on a VSM with the applied field of -8 kOe to 8 kOe at room temperature (300 K). As shown in Fig. 10a, the S-like curves exhibited distinctly symmetrical hysteresis loops and showed ferromagnetic behavior: the M_s values for pure Fe$_3$O$_4$ and the PONs$_{(1/3)}$ composite were 69.7 emu g^{-1} (32 Oe) and 14.1 emu g^{-1} (30 Oe), respectively. The decrease in magnetization of the PONs$_{(1/3)}$ composite may be caused by the coating of the BiOI shell, which reduces the magnetite fraction in each microsphere.[35] Nevertheless, as shown in Fig. 10c, the well-dispersed PONs$_{(1/3)}$ powders could be separated rapidly from water within 20 s, demonstrating that the as-prepared composite possesses a good response towards the external magnetic field. The specific magnetic property of the PONs$_{(1/3)}$ composite provides a possibility for effective separation and
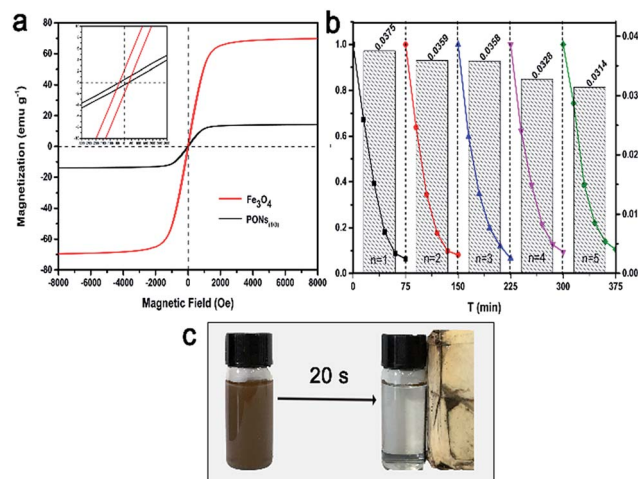
recycling. To verify the stability of the catalyst during photodegradation, a series of successive experiments with MO as the target pollutant were conducted. As depicted in Fig. 10b, the rate constants, k, of each cycle were calculated to be 0.0375, 0.0359, 0.0358, 0.0328, and 0.0314, respectively. It is worth mentioning that there is a 16% difference in the rate constant values between the first cycle and the fifth cycle. To investigate the reason for the decline in catalytic efficiency and to validate the stability of the photocatalysts, XRD and thermogravimetric (TG) investigations were carried out. In Fig. S1,† it can be seen by comparing the XRD patterns of samples before and after reactions that the photocatalytic process had little impact on the phase composition. However, after five cycles of photocatalytic reactions, the mass fraction of BiOI had changed from 90% to 80%, as shown in Fig. S2.† It can be speculated that the catalyst deactivation could be attributed to the small release of BiOI during the separation and recycling process. In general, as an effective separation and recycling catalyst, the PONs$_{(1/3)}$ composite is still very stable and reliable.

3.3 Proposed mechanism

Generally, there are three possible reaction mechanisms for the photodegradation of organics by semiconductors, namely (i) photocatalysis, (ii) photolysis, and (iii) dye photosensitization.[41] However, the decomposition of phenol by photolysis is negligible; degradation caused by photolysis under visible light in a blank test is not observable, as shown in Fig. 11a. Since phenol is one of the organics with no indirect dye photosensitization, the effect of dye photosensitization may also be neglected. Therefore, photocatalysis can be considered as the only possible reaction mechanism for the degradation of phenol over PONs$_{(1/3)}$.

To detect the active species, a series of trapping experiments during photocatalysis were performed. The radical trapping agents include BQ (1 mM, a scavenger of $\cdot$O$_2^-$), EDTA-2Na (1 mM, a scavenger of h$^+$), and methanol (1 mM, a scavenger
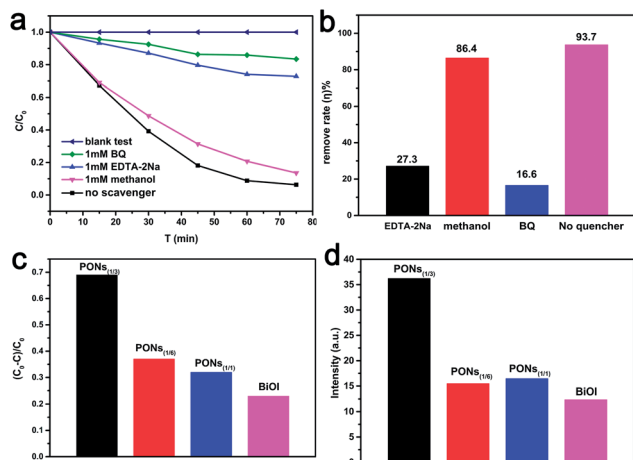
Fig. 11 (a) Trapping experiments for detecting the active species over PONs$_{(1/3)}$; (b) removal efficiency of MO over PONs$_{(1/3)}$ with the addition of different scavengers; (c) nitroblue tetrazolium (NBT) transforming efficiencies; (d) hydroxyterephthalic acid (TA-OH) fluorescence intensities of PONs$_{(1/3)}$, PONs$_{(1/1)}$, PONs$_{(1/6)}$ and BiOI.
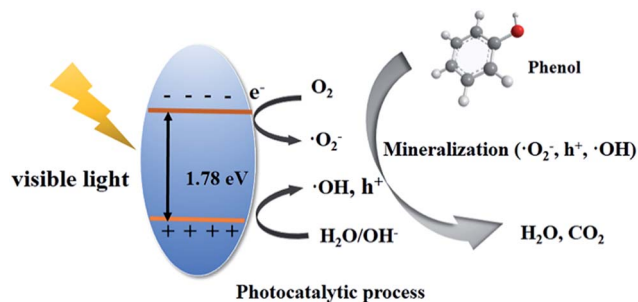

Fig. 12 Schematic illustration of the proposed photocatalytic degradation mechanism of phenol over PONs$_{(1/3)}$ under visible light.

of $\cdot$OH), respectively.[38] As shown in Fig. 11b, the photodegradation was remarkably prohibited when the BQ radical scavenger (scavenger of $\cdot$O$_2^-$) was introduced. Besides, the degradation efficiency was relatively less affected by EDTA-2Na (scavenger of h$^+$) or methanol (scavenger of $\cdot$OH). The above trapping experiment results suggest that photogenerated $\cdot$O$_2^-$ play a chief role, while the h$^+$ and $\cdot$OH play minor roles in the photocatalytic system.

To verify the aforementioned results and quantitatively compare the amounts of radicals generated on the as-prepared samples, the NBT (detection agent for $\cdot$O$_2^-$) transformation and TA-PL probing techniques were applied with 1 h visible-light irradiation during the photocatalytic reaction.[50] As shown in Fig. 11c, the time-resolved absorption spectra of NBT show that the transformation percentage of NBT catalysed by the PONs$_{(1/3)}$ was greater than that for the other samples. Moreover, the NBT conversion percentage by PONs$_{(1/3)}$ was up to 69%, which further demonstrates that the $\cdot$O$_2^-$ radicals serving as active species play crucial roles in the degradation process. As shown in Fig. 11d, the fluorescence intensity of TA-OH over PONs$_{(1/3)}$ was higher than that with other samples, although all the peak intensities were very weak, indicating that $\cdot$OH radicals only play minor roles in the catalytic process.

Accordingly, a possible mechanism for the PONs$_{(1/3)}$ photocatalyst can be proposed; the above results clearly suggest that the degradation of phenol is primarily attributed to $\cdot$O$_2^-$, h$^+$ and $\cdot$OH. As aforementioned, the as-prepared catalyst is an n-type semiconductor (Mott–Schottky plots), and hence the BiOI coating proves to be an excellent platform to transfer electrons. Those electrons consequently reduce the O$_2$ molecules adsorbed on the catalyst surface into superoxide radicals of $\cdot$O$_2^-$. Jiang *et al.* reported that $\cdot$O$_2^-$ is the most important active species in the photocatalytic degradation of phenol by BiOI.[51] Theoretically, $\cdot$OH is an extremely strong oxidant with nonselective characteristics.[52] It is proposed that the probability of

forming $\cdot$OH should be much lower than that for $\cdot$O$_2^-$ on account of the fact that the redox potential of Bi^V/Bi^{III} (1.59 eV) is more negative than the standard potential of $\cdot$OH/OH$^-$ (2.38 eV).[53] Since the limited transformation reaction of h$^+$ + OH$^-$ → $\cdot$OH, a fraction of h$^+$ can participate in the oxidization. On the basis of the above mentioned reason, it is proposed that under visible-light irradiation, electron–hole pairs are firstly generated over the BiOI coatings. Then phenol adsorbed on the surface of the catalyst is oxidized by the activated oxygen $\cdot$O$_2^-$, h$^+$ and $\cdot$OH species to form the corresponding intermediate which is further oxidized into degradation products as shown in Fig. 12.

4.   Conclusions

In summary, we have constructed a novel photocatalyst (PONs) through a simple and direct precipitation method, which exhibits substantially enhanced photocatalytic activity as compared to pure BiOI and Fe$_3$O$_4$/BiOI. Under visible-light irradiation, PONs possessed prominent photocatalytic activity toward phenol and could eliminate more than 90% phenol within 5 h. Such enhanced photoactivity is due to the unique synergistic effect between the magnetic core and BiOI shell of the catalyst. Additionally, PONs have satisfactory cycling stability and superior magnetic recovery performance. This work not only paves a way for the design of efficient photocatalysts with magnetic cores and photocatalyst shells, but also opens up new possibilities for photocatalysts with favorable durability and recyclability in practical applications.

Conflict of interest

There are no conflicts of interest to declare.

Acknowledgements

Notes and references

1 A. Fujishima, *Nature*, 1972, **238**, 37–38.

2 J. Tang, Z. Zou and J. Ye, *Angew. Chem., Int. Ed.*, 2004, **43**, 4463–4466.

3 S. H. S. Chan, T. Yeong Wu, J. C. Juan and C. Y. Teh, *J. Chem. Technol. Biotechnol.*, 2011, **86**, 1130–1158.

4 C. Hachem, F. Bocquillon, O. Zahraa and M. Bouchy, *Dyes Pigm.*, 2001, **49**, 117–125.

5 L. Ren, Y. Li, J. Hou, X. Zhao and C. Pan, *ACS Appl. Mater. Interfaces*, 2014, **6**, 1608–1615.

6 Y. C. Pu, G. Wang, K. D. Chang, Y. Ling, Y. K. Lin, B. C. Fitzmorris, C. M. Liu, X. Lu, Y. Tong, J. Z. Zhang, Y. J. Hsu and Y. Li, *Nano Lett.*, 2013, **13**, 3817–3823.

7 A. W. Xu, Y. Gao and H. Q. Liu, *J. Catal.*, 2002, **207**, 151–157.

8 R. Leary and A. Westwood, *Carbon*, 2011, **49**, 741–772.

9 X. Wang, S. Blechert and M. Antonietti, *ACS Catal.*, 2012, **2**, 1596–1606.

10 Y. Qu, L. Liao, R. Cheng, Y. Wang, Y. C. Lin, Y. Huang and X. Duan, *Nano Lett.*, 2010, **10**, 1941–1949.

11 Y. Guo, H. Huang, Y. He, N. Tian, T. Zhang, P. K. Chu, Q. An and Y. Zhang, *Nanoscale*, 2015, **7**, 11702–11711.

12 J. Jiang, X. Zhang, P. Sun and L. Zhang, *J. Phys. Chem. C*, 2011, **115**, 20555–20564.

13 H. Huang, K. Xiao, K. Liu, S. Yu and Y. Zhang, *Cryst. Growth Des.*, 2016, **16**, 221–228.

14 L. Sun, L. Xiang, X. Zhao, C. J. Jia, J. Yang, Z. Jin, X. Cheng and W. Fan, *ACS Catal.*, 2015, **5**, 3540–3551.

15 F. Tian, H. Zhao, Z. Dai, G. Cheng and R. Chen, *Ind. Eng. Chem. Res.*, 2016, **55**, 4969–4978.

16 Y. Wang, K. Deng and L. Zhang, *J. Phys. Chem. C*, 2011, **115**, 14300–14308.

17 X. Xiao and W. D. Zhang, *J. Mater. Chem.*, 2010, **20**, 5866.

18 X. Qian, D. Yue, Z. Tian, M. Reng, Y. Zhu, M. Kan, T. Zhang and Y. Zhao, *Appl. Catal., B*, 2016, **193**, 16–21.

19 Y. Zhang, N. Zhang, Z. R. Tang and Y.-J. Xu, *Chem. Sci.*, 2013, **4**, 1820–1824.

20 L. Chen, Q. Zhang, R. Huang, S. F. Yin, S. L. Luo and C. T. Au, *Dalton Trans.*, 2012, **41**, 9513–9518.

21 C. Li, S. Wang, T. Wang, Y. Wei, P. Zhang and J. Gong, *Small*, 2014, **10**, 2783–2790.

22 H. Li, K. Yu, X. Lei, B. Guo, H. Fu and Z. Zhu, *J. Phys. Chem. C*, 2015, **119**, 22681–22689.

23 H. S. Park, K. E. Kweon, H. Ye, E. Paek, G. S. Hwang and A. J. Bard, *J. Phys. Chem. C*, 2011, **115**, 17870–17879.

24 W. Zhao, Y. Wang, Y. Yang, J. Tang and Y. Yang, *Appl. Catal., B*, 2012, **115–116**, 90–99.

25 P. Madhusudan, J. Ran, J. Zhang, J. Yu and G. Liu, *Appl. Catal., B*, 2011, **110**, 286–295.

26 J. Tian, P. Hao, N. Wei, H. Cui and H. Liu, *ACS Catal.*, 2015, **5**, 4530–4536.

27 C. Yu, Z. Wu, R. Liu, D. D. Dionysiou, K. Yang, C. Wang and H. Liu, *Appl. Catal., B*, 2017, **209**, 1–11.

28 Y. Huang, H. Li, M. S. Balogun, W. Liu, Y. Tong, X. Lu and H. Ji, *ACS Appl. Mater. Interfaces*, 2014, **6**, 22920–22927.

29 L. Ye, L. Tian, T. Peng and L. Zan, *J. Mater. Chem.*, 2011, **21**, 12479–12484.

30 X. Zhang, L. Zhang, T. Xie and D. Wang, *J. Phys. Chem. C*, 2009, **113**, 7371–7378.

31 M. Shekofteh-Gohari and A. Habibi-Yangjeh, *J. Colloid Interface Sci.*, 2016, **461**, 144–153.

32 S. Xuan, W. Jiang, X. Gong, Y. Hu and Z. Chen, *J. Phys. Chem. C*, 2009, **113**, 553–558.

33 Z. Zhu, Z. Lu, D. Wang, X. Tang, Y. Yan, W. Shi, Y. Wang, N. Gao, X. Yao and H. Dong, *Appl. Catal., B*, 2016, **182**, 115–122.

34 S. Kumar, T. Surendar, B. Kumar, A. Baruah and V. Shanker, *J. Phys. Chem. C*, 2013, **117**, 26135–26143.

35 G. Xi, B. Yue, J. Cao and J. Ye, *Chemistry*, 2011, **17**, 5145–5154.

36 Y. Wang, S. Li, X. Xing, F. Huang, Y. Shen, A. Xie, X. Wang and J. Zhang, *Chemistry*, 2011, **17**, 4802–4808.

37 M. Zhu and G. Diao, *J. Phys. Chem. C*, 2011, **115**, 18923–18934.

38 S. Zhong, W. Jiang, M. Han, G. Liu, N. Zhang and Y. Lu, *Appl. Surf. Sci.*, 2015, **347**, 242–249.

39 H. Huang, Y. He, R. He, Z. Lin, Y. Zhang and S. Wang, *Inorg. Chem.*, 2014, **53**, 8114–8119.

40 S. Y. Chou, W. H. Chung, L. W. Chen, Y. M. Dai, W. Y. Lin, J. H. Lin and C. C. Chen, *RSC Adv.*, 2016, **6**, 82743–82758.

41 Y. H. Lee, Y. M. Dai, J. Y. Fu and C. C. Chen, *Mol. Catal.*, 2017, **432**, 196–209.

42 S.-Y. Chou, C. C. Chen, Y. M. Dai, J. H. Lin and W. W. Lee, *RSC Adv.*, 2016, **6**, 33478–33491.

43 S.-T. Huang, Y.-R. Jiang, S. Y. Chou, Y.-M. Dai and C.-C. Chen, *J. Mol. Catal. A: Chem.*, 2014, **391**, 105–120.

44 X. Zhou, D. Xu, J. Lu and K. Zhang, *Chem.–Eur. J.*, 2015, **266**, 163–170.

45 Z. Ai, W. Ho, S. Lee and L. Zhang, *Environ. Sci. Technol.*, 2009, **43**, 4143–4150.

46 J. Li, L. Cai, J. Shang, Y. Yu and L. Zhang, *Adv. Mater.*, 2016, **28**, 4059–4064.

47 H. Huang, X. Han, X. Li, S. Wang, P. K. Chu and Y. Zhang, *ACS Appl. Mater. Interfaces*, 2015, **7**, 482–492.

48 W. W. Lee, C. S. Lu, C. W. Chuang, Y. J. Chen, J. Y. Fu, C. W. Siao and C. C. Chen, *RSC Adv.*, 2015, **5**, 23450–23463.

49 K. V. Kumar, K. Porkodi and F. Rocha, *Catal. Commun.*, 2008, **9**, 82–84.

50 L. Ye, J. Liu, Z. Jiang, T. Peng and L. Zan, *Appl. Catal., B*, 2013, **142–143**, 1–7.

51 Y. R. Jiang, S. Y. Chou, J.-L. Chang, S. T. Huang, H.-P. Lin and C. C. Chen, *RSC Adv.*, 2015, **5**, 30851–30860.

52 H. L. Chen, W. W. Lee, W. H. Chung, H.-P. Lin, Y. J. Chen, Y. R. Jiang, W. Y. Lin and C. C. Chen, *J. Taiwan Inst. Chem. Eng.*, 2014, **45**, 1892–1909.

53 Y. R. Jiang, H. P. Lin, W. H. Chung, Y. M. Dai, W. Y. Lin and C. C. Chen, *J. Hazard. Mater.*, 2015, **283**, 787–805.